Geophys. J. Int. (1998) **134**, 449–459

Global derivation of marine gravity anomalies from Seasat, Geosat, ERS-1 and TOPEX/POSEIDON altimeter data

Cheinway Hwang,[1] Eu-Chi Kao[1] and Barry Parsons[2]

[1] *Department of Civil Engineering, National Chiao Tung University, Hsinchu, Taiwan. E-mail: hwang@geodesy.cv.nctu.edu.tw*

[2] *Department of Earth Sciences, University of Oxford, Oxford, UK*

Accepted 1998 February 20. Received 1998 February 12; in original form 1997 September 23

SUMMARY

Marine gravity anomalies over the area 82°S to 82°N and 0°E to 360°E on a 2′ × 2′ grid have been derived from Seasat, Geosat, ERS-1 and TOPEX/POSEIDON altimeter data. The inverse Vening Meinesz formula with a 1-D FFT method was used to compute gravity anomalies from gridded north–south and west–east geoid gradients, in a remove–restore procedure with the EGM96 gravity model as the reference field. This paper presents a new gridding technique and an altimeter data management system that help to extract data efficiently. In the 12 areas where ship-measured gravity and satellite-derived gravity were compared, rms agreements of 5–14 mgal were obtained. Special discussions of the gravity anomalies over selected inland seas, the Arctic, Antarctica and coastal waters are presented. The derived gravity anomalies show detailed tectonic structures of the world ocean. The global data set will be continuously updated with more altimeter data included in the derivation.

Key words: gravity anomalies, satellite geodesy.

1 INTRODUCTION

Since the Seasat mission of 1978, global marine gravity anomalies of different accuracies and spatial resolutions have been derived from satellite altimetry. In these gravity derivations, three typical procedures are (1) correcting sea surface heights from altimetry for orbital errors by minimizing crossover differences, and then deriving gravity anomalies from sea surface heights using least-squares collocation (e.g. Hwang 1989; Rapp & Basic 1992); (2) adjusting sea surface heights as in (1), and then transforming sea surface heights to gravity anomalies in the spectral domain (e.g. Knudsen & Andersen 1997); (3) differentiating along-track sea surface heights to get sea surface gradients, calculating the east and north components of the sea surface gradient on a regular grid, and then transforming the two components to gravity anomalies in the spectral domain (e.g. Haxby *et al.* 1983; Sandwell & Smith 1997). In this paper, we will use the latter procedure, but adopt a new gridding method and a new gravity conversion formula derived by Hwang (1998). Furthermore, we will attempt to use all altimeter data—Seasat, Geosat Exact Repeat Mission (Geosat/ERM), Geosat Geodetic Mission (Geosat/GM), ERS-1 35-day Repeat Mission (ERS-1/35-day), ERS-1/GM and TOPEX/POSEIDON (T/P)—in the gravity derivation. With altimeter data from such a variety of satellite missions, a good data management system is important and will be discussed. The quality of the derived gravity anomalies will be evaluated by comparison with shipborne gravity data over 12 selected, tectonically active regions. The ultimate goal of this work is to make a global marine-gravity data set available to the scientific community.

2 THE ALTIMETER DATA FOR MARINE GRAVITY DETERMINATION

Table 1 summarizes information about the altimeter data used in this work. Despite the fact that the quality of the measurements from different altimeter missions varies considerably, we have attempted to use all existing data. By weighting the different data sets according to their uncertainties, an optimal combination of them is possible. The Seasat data were collected in 1978 and have the poorest quality. However, by an outlier rejection method, the bad Seasat data may be eliminated while the good Seasat data are retained and contribute to improving the spatial resolution of the gravity field. In terms of point data, T/P has the best quality of all, but it contributes little to the spatial resolution owing to its large cross-track spacing. The Geosat/ERM geophysical data records (GDRs) we have are based on the GEM-T2 orbit (Cheney *et al.* 1991). The Geosat/GM GDRs we have are from NOAA, which used the Naval Surface Weapons Center orbit and the Schwideriski tide model (Cheney *et al.* 1991). For this work, the Schwideriski tide model in the Geosat/GM GDRs was replaced by the Center for Space Research (CSR) 3.0 tide model (Eanes & Bettadpur 1995). The sea surface heights in our Geosat/GM database were prepared at 2 per second (Hz) by least-squares

Table 1. Information about the satellite altimeter data used in the present analysis.

Satellite	Seasat	Geosat	ERS-1	TOPEX/POSEIDON
Mission	-	ERM/GM	35-day/GM	ERM
Inclination angle (degree)	108	108/108	98.5/98.5	66
Repeat or mission period (day)	3-17	17/535	35/168	10
No. of cycles	-	62/1	18/2	111
Data duration (year)	0.25	2/1.5	1.5/0.92	3
Cross-track spacing (km)	165	165/4	80/8	280
Along-track spacing (km)	6.7	6.7/3.3	6.7/6.7	5.8

fitting of a second-degree polynomial to the 10 Hz data in the GDRs. In estimating the polynomial coefficients, the τ-test (Pope 1976) was used to reject the bad values of sea surface height in an iterative procedure. The standard deviations of the estimated 2 Hz sea surface heights were also computed and are given in Table 2. The standard deviations in Table 2, which are mostly below 3 cm in the open oceans, reflect only the random part of the altimeter error, and do not include systematic errors from orbits and geophysical corrections. We have identified at least six passes of Geosat/GM with abnormal variations in sea surface height but still with small standard deviations. Use of these tracks yielded an unrealistic signature of gravity, so these 'bad' tracks were simply ignored in our computations. The ERS-1/GM data we used are from Le Traon *et al.* (1995), who refined the ERS-1/GM sea surface heights using T/P sea surface heights with a crossover adjustment technique. Furthermore, the CSR 3.0 tide model was used to correct the ERS-1/GM sea surface heights. In order of increasing data density, the sequence is T/P, Geosat, Seasat, ERS-1/35-day, ERS-1/GM and Geosat/GM.

In computing gravity anomalies from satellite altimeter data, normally two types of data are used—sea surface heights and sea surface gradients, which, after removing the effect of the sea surface topography, are geoidal undulations and geoid gradients, respectively. Because of factors such as orbit error and inconsistency in the satellite orbit frame, the sea surface heights from different satellite missions need to be adjusted to a 'standard' surface. In this regard, perhaps the sea surface heights from T/P can serve as a standard surface because of its highly accurate orbit. Failure to adjust properly the sea surface heights from different satellite missions will result in track patterns in the derived gravity anomalies (e.g. Hwang 1989; Rapp & Basic 1992). One way to avoid crossover adjustment of sea surface heights while minimizing the effect of systematic errors in altimetry is to make use of geoid gradients (Hwang 1997). In this study, the basic observables we used were along-track geoid gradients computed from

$$e(\alpha) = \frac{\partial h}{\partial s}, \tag{1}$$

where α is the azimuth, h is the geoidal height (assuming no sea surface topography) and s is the along-track distance. Using gradients is comparable to using differenced phase observables in the Global Positioning System (GPS), where the systematic errors due to the orbits and to ionospheric propagation, for example, can be reduced. In particular, the long-wavelength errors will have much less effect on geoid gradient than on sea surface height. A drawback in using the geoid gradient is that short-wavelength noise is enhanced because of differencing, but this can be overcome by proper filtering. Furthermore, geoid gradients from repeat cycles of the Geosat/ERM, ERS-1/35-day and T/P missions were stacked to reduce data noise. The stacked gradients were obtained at whole numbers of seconds after equator crossings by differencing along-track sea surface heights and then averaging over a number of passes. Since a pass from any repeating cycle will repeat the same location with a 1 km accuracy, the positions of the stacked gradients are simply the averaged positions of the passes used. It has been noted that the tide model error in the stacked gradients can be reduced substantially (Hwang 1997).

Table 2. Standard deviations of sea surface heights measured by Geosat/GM in areas of different depths.

Depth (m)	Std. dev. (m)
0-500	0.076
500-1000	0.069
1000-2000	0.062
2000-3000	0.038
3000-4000	0.031
4000-5000	0.033
5000-6000	0.018
6000-7000	0.009
7000-	0.017

3 ALTIMETER DATA MANAGEMENT

An important element in the simultaneous use of altimeter data from the six missions listed in Table 1 is a fast method to extract data for a given computational area. Here we present a method based on the equator-crossing longitude for each pass. Here a pass is defined as a segment of an orbital arc between the two extreme latitudes of a satellite mission. First, the data for each mission is broken up into separate passes, and one file stores data from one pass only. For the repeat missions Geosat/ERM, ERS-1/35-day and T/P, the equator-crossing longitudes are easily found by using the equator-crossing longitudes of the first passes and the repeat periods. For the non-repeat missions, the equator-crossing longitude of a pass, λ_x, was estimated from (Fig. 1)

$$\lambda_x = \lambda + \varepsilon[\lambda_T - T(\omega - \dot{\Omega})], \tag{2}$$

where T is the time since the equator-crossing, ω is the Earth's mean rotational velocity, $\dot{\Omega}$ is the secular precession rate of the orbital plane and

$$\varepsilon = \begin{cases} -1 & \text{for an ascending track,} \\ 1 & \text{for a descending track,} \end{cases} \tag{3}$$

$$\lambda_T = \arctan(\cos I \tan u), \tag{4}$$

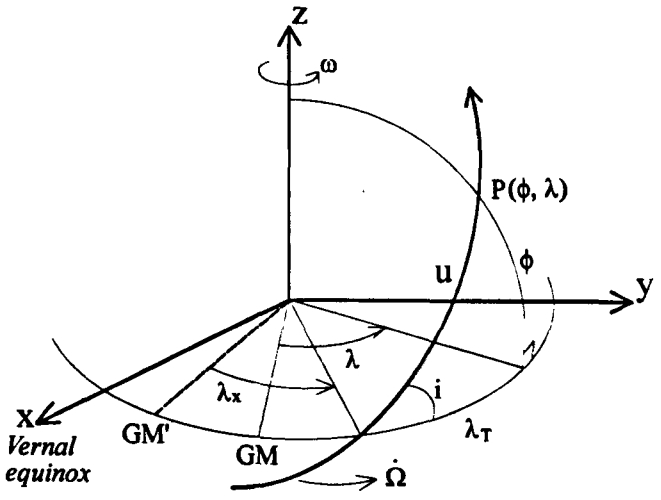

Figure 1. Geometry to determine the equator-crossing longitude of a satellite pass. GM' is the position of the Greenwich meridian when the satellite is crossing the equator. When the satellite travels to point P(ϕ, λ), the Greenwich meridian moves to GM.

with I and u being the inclination angle of the orbital plane and the argument of latitude, respectively; u is given by

$$u = \arcsin\left(\frac{\sin\phi}{\sin I}\right), \tag{5}$$

where ϕ is the geocentric latitude. The velocity of u can be computed from (Kaula 1966)

$$\dot{u} = n + \frac{3nC_{20}a_e^2}{4(1-e^2)^2a^2}(1-5\cos^2 I) - \frac{3nC_{20}a_e^2}{4(1-e^2)^{3/2}a^2}(3\cos^2 I - 1), \tag{6}$$

where C_{20} is the second zonal harmonic coefficient, a and e are the semi-major axis and the eccentricity of the orbital ellipse, a_e is the semi-major axis of a reference ellipsoid for the Earth and n is the mean angular velocity of the satellite around the Earth, defined by

$$n = \sqrt{\frac{GM}{a^3}}, \tag{7}$$

where GM is the Earth's gravitational constant.

The time since the equator-crossing is then

$$T = \frac{u}{\dot{u}}. \tag{8}$$

Finally, the secular precession rate of the orbital plane is

$$\dot{\Omega} = \frac{3nC_{20}a_e^2}{2(1-e^2)^2a^2}\cos I. \tag{9}$$

Since formulae such as eq. (6) are only approximate, for each single pass we computed the equator-crossing longitudes from all data points along the pass and then took the average to ensure a most probable equator-crossing longitude for that pass. In this way we have established tables of equator-crossing longitudes for Seasat, Geosat/GM and ERS-1/GM in our altimeter database.

Using the equator-crossing longitude of a pass and the geographical borders of the given area, the two longitudes λ_n and λ_s where the pass intersects the northern and southern borders, respectively, can be determined using eq. (2) in reverse. Fig. 2 shows the four cases in which a pass goes through an area for $I < 90°$. For example, for an ascending pass, λ_n and λ_s in the case on the right of Fig. 2 satisfy the condition $\lambda_n >$ longitude of the eastern border and $\lambda_s <$ longitude of the western border. Having selected the passes going through the area, the corresponding files are then opened for further data extraction using the geographical borders. Extracting data in this way can save a significant amount of computer time.

4 USE OF REFERENCE FIELD AND SEA SURFACE TOPOGRAPHY MODEL

In the gravity computations, we use the remove–restore procedure, for which a reference gravity field is needed. The choice of reference field has been somewhat arbitrary in the literature, e.g. Sandwell & Smith (1997), Hwang (1989) and Rapp & Basic (1992) chose to use degree 70, 180 and 360 fields, respectively (note that the gravity models are also different). Wang's (1993) theory suggests the use of a reference field of the highest degree, provided that the geopotential coefficients are properly scaled by the factor S_n given by

$$S_n = \frac{c_n}{c_n + \varepsilon_n}, \tag{10}$$

where c_n and ε_n are the degree variance and the error degree variance of the chosen reference field. Wang's theory was tested by Hwang & Parsons (1996) and, in the case of OSU91A (Rapp, Wang & Pavlis 1991), the scaling factors improve

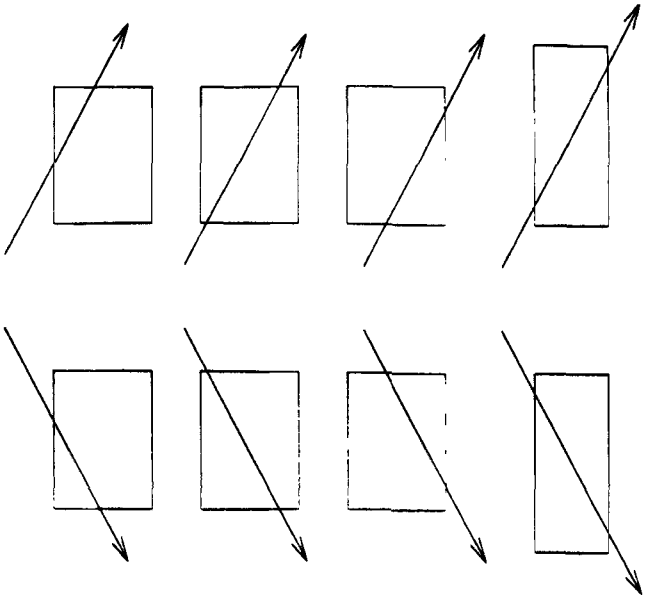

Figure 2. The four cases in which a satellite's path goes through a given region (shown as a box). The first row is for an ascending track and the second row is for a descending track.

slightly the accuracy of the computed gravity anomalies. In this study, we chose to use the EGM96 model (Lemoine *et al.* 1997) to degree 360 as the reference field. We did tests at the Reykjanes Ridge and the South China Sea (see below) to see whether the scaling factor S_n is necessary. The results show that the use of S_n does not increase the accuracy of the computed gravity anomalies in the two test areas. This is perhaps due to the fact that EGM96's high-degree coefficients are substantially improved compared to OSU91A, since S_n has a larger effect on the high-degree coefficients than on the low-degree ones.

Another effect that needs investigating is that of sea surface topography on the derived gravity values. In theory, both the time-varying and the quasi-stationary sea surface topography should be removed from the altimeter sea surface heights in order to get geoidal heights. Here we investigate only the effect of the quasi-stationary sea surface topography. For this investigation we computed gravity anomalies in an area near the Kuroshio Extension using altimeter data, both with and without the Levitus (1982) sea surface topography removed. Fig. 3 shows the difference between the gravity anomalies obtained in the two cases. In this area the average slope of the sea surface topography is about 0.5 μrad and the slope is mostly along the north–south direction (see also Hwang 1997). The sea surface topography slopes resulted in a systematic difference of 0.1 mgal. We believe that removing the Levitus sea surface topography will at least reduce the effect of long-wavelength sea surface topography in areas of energetic currents, such as the Gulf Stream area and the Kuroshio area. We have removed the Levitus sea surface topography values from the sea surface heights before gravity computation here.

5 REJECTING BAD GEOID GRADIENTS

Use of geoid gradients may reduce the effect of systematic errors but other problems still exist. For example, if a satellite frame in one of the six missions is significantly incompatible with the others, the incompatibility, depending on the

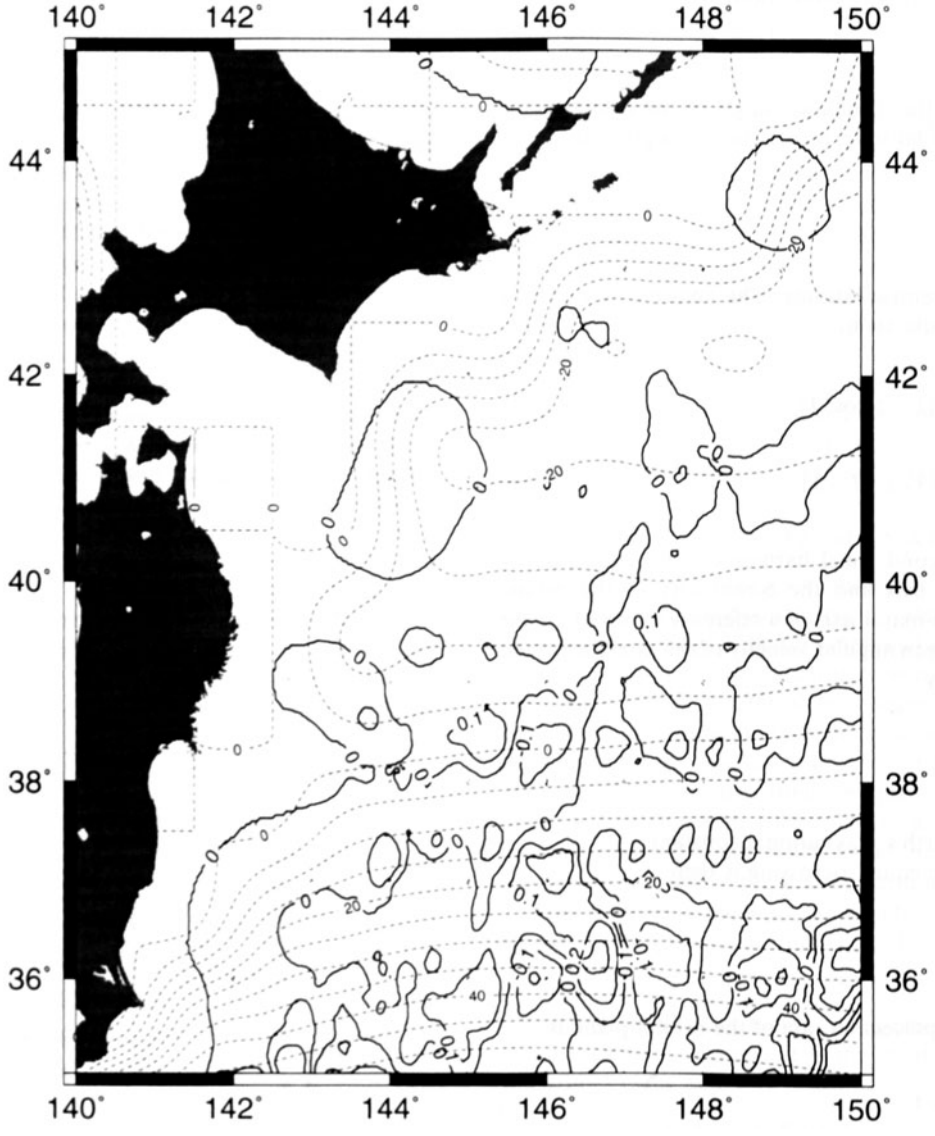

Figure 3. Difference in the computed gravity anomalies using altimeter data with and without the Levitus sea surface topography removed (solid lines). Also plotted is the Levitus sea surface topography (dashed lines). Contour intervals for gravity anomaly and sea surface topography are 0.1 mgal and 5 cm, respectively.

geographical location, will make the data from this mission appear as outliers in the presence of data from the other missions. Therefore, to have a consistent data set when using the data from the six missions, outlier rejection was performed. The rejection was done on a point-by-point basis. At a grid point where the gravity anomaly was wanted, the gradients within a cell centred at this point were used to form the observation equations

$$\varepsilon_i + v_i = \xi \cos \alpha_i + \eta \sin \alpha_i, \quad \text{for } i = 1, \ldots, n, \tag{11}$$

where ε_i is the ith observed gradient with the azimuth α_i, and ξ and η are the north and east gradient components. A typical cell size for testing for outliers was $4' \times 4'$, which contains about 12 points. The weight of a gradient was set to be

$$P_i = \frac{1}{d_i^2 \sigma_i^2}, \tag{12}$$

where d_i is the distance to the grid point and σ_i is the standard deviation of the gradient. Using the least-squares principle $\Sigma_{i=1}^{n} P_i v_i^2 =$ a minimum, we solved for ξ and η. A gradient ε_i was rejected if the following condition was met:

$$\frac{|v_i|}{\sigma_{v_i}} > \tau_c, \tag{13}$$

where τ_c is the critical τ value (Pope 1976), and

$$\sigma_{v_i} = \sqrt{\frac{\mathbf{v}^T \mathbf{p} \mathbf{v}}{n P_i}}, \tag{14}$$

where $\mathbf{v}$ is a vector holding the residuals and $\mathbf{p}$ is a diagonal matrix holding the weights. We have used a 99 per cent confidence level for τ_c. We selected 12 tectonically active areas, as shown in Fig. 4, to test our outlier rejection method. These 12 areas are also used for gravity comparison below. Table 3 shows the percentages of rejected gradients in the 12 areas. The rejected gradients come almost exclusively from the non-repeat missions. The bad data from Seasat and ERS-1/GM that were pointed out by Hwang (1997) in many parts of the oceans have disappeared in the cleaned data set. Unfortunately, this method will not work properly if there are not sufficient data to let the theory of outlier rejection hold, especially near coastal waters and areas with sparse data. Outlier rejection also reduces the time for gridding because the amount of data is reduced. The results from gravity comparisons show that outlier rejection indeed improves the accuracies of the computed gravity anomalies over both deep and shallow seas.

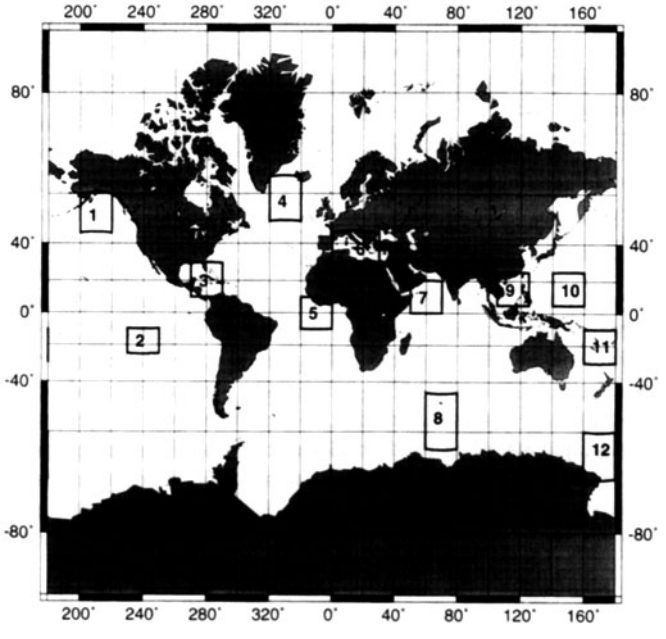

Figure 4. Locations of the twelve areas where outlier rejection was tested, and satellite-derived and shipborne gravity anomalies were compared.

Table 3. Statistics of outlier rejection in the 12 areas.

Area	Name	Total	Rejected	Percentage
1	Alaska Abyssal	596329	33350	5.6
2	East Pacific Rise	754522	33315	4.4
3	Caribbean Sea	547471	33301	6.1
4	Reykjanes Ridge	665557	34245	5.1
5	Mediterranean Sea	810963	29710	3.7
6	Carlsberg Ridge	241066	16979	7.0
7	Sierra Leone Basin	831157	40266	4.8
8	Kerguelen Plateau	796664	45866	5.8
9	South China Sea	468891	28768	6.1
10	Mariana Trench	458452	41970	9.2
11	Fiji Plateau	914693	41163	4.5
12	Ross Sea	366315	26121	7.1

6 COMPUTING GRAVITY ANOMALIES USING INVERSE VENING MEINESZ FORMULA WITH 1-D FFT

Many methods for deriving gravity anomalies from altimeter data exist. A realistic method for a global-scale computation will make use of the fast Fourier transform technique. In this paper, we choose to use the inverse Vening Meinesz formula for gravity derivation. The inverse Vening Meinesz formula reads (Hwang 1998)

$$\Delta g(p) = \frac{\gamma_0}{4\pi} \iint_{\sigma} H'(\xi_q \cos \alpha_{qp} + \eta_q \sin \alpha_{qp}) d\sigma_q, \tag{15}$$

where γ_0 is the mean gravity; α_{qp} is the azimuth from q to p; ξ_q and η_q are the north and east components of the deflection of the vertical, which has the opposite sign to geoid gradient; σ is the unit sphere; and H' is a kernel function defined as

$$H' = \frac{\cos(\psi/2)}{2 \sin(\psi/2)} \left(-\frac{1}{\sin(\psi/2)} + \frac{3 + 2 \sin(\psi/2)}{1 + \sin(\psi/2)} \right), \tag{16}$$

with ψ being the spherical distance. In theory, in order to determine the gravity anomaly at any given point, knowledge of the deflections over the entire unit sphere is required. However, owing to the use of a high-degree reference field, only data within a limited area surrounding the computational point are needed. If the data are given on a regular geographical grid, surface integrals such as eq. (15) can be rigorously evaluated by the 1-D fast Fourier transform (FFT) method (Haagmans, de Min & von Gelderen 1993), which does the computation on a parallel basis. Thus, the discrete formula for

gravity derivation we used was

$$\Delta g_{\phi_p} = \frac{\gamma_0 \Delta\phi \Delta\lambda}{4\pi} F_1^{-1} \sum_{\phi_q=\phi_1}^{\phi_2} \{F_1[\bar{H}'(\Delta\lambda_{qp}) \cos \alpha_{qp}] F_1(\xi_{\cos}) + F_1[\bar{H}'(\Delta\lambda_{qp}) \sin \alpha_{qp}] F_1(\eta_{\cos})\}, \quad (17)$$

where p is the 'fixed' point and q is the 'dummy' or 'running' point, ϕ_p is the latitude of the parallel along which gravity anomalies are to be computed, ϕ_1 and ϕ_2 are the latitudes of the southernmost and the northernmost parallels within a cap of size S, $\Delta\phi$ and $\Delta\lambda$ are the grid intervals in latitude and longitude, λ_{qp} is the difference in longitude, F_1 is the 1-D FFT, and $\xi_{\cos}$, $\eta_{\cos}$, $\bar{H}'$ are defined by

$$\xi_{\cos} = \xi \cos\phi, \quad \eta_{\cos} = \eta \cos\phi, \quad (18)$$

$$\bar{H}' = \begin{cases} H' & \text{if } \psi \le S, \\ 0 & \text{if } \psi > S. \end{cases} \quad (19)$$

Owing to the rapid decay of the kernel function and the small magnitude of the residual gradients, it was found that there is practically no contribution from data outside a cap of 110 km (about 1). Furthermore, we employed 100 per cent zero paddings in the 1-D FFT to avoid aliasings. We also added the innermost-zone effect that accounts for the contribution of the geoid gradients immediately surrounding the grid point. The innermost-zone effect is computed from

$$\Delta g_i = \frac{s_0 \gamma_0}{2}(\xi_y + \eta_x), \quad (20)$$

where s_0 is the radius of the innermost zone, γ_0 is the mean gravity, $\xi_y = \partial\xi/\partial y$ and $\eta_x = \partial\eta/\partial y$, with x and y being the rectangular coordinates along the east and north directions. By using the planar approximation, the inverse Vening Meinesz formula in the spectral domain can be derived and has been used by many researchers (e.g. Sandwell & Smith 1997; Hwang & Parsons 1996).

7 GRIDDING THE NORTH AND EAST COMPONENTS OF GEOID GRADIENTS

For the 1-D FFT method of gravity derivation, the north and east gradient components must be prepared on a regular grid using the along-track gradients computed from eq. (1). Owing to the different data qualities, we used least-squares collocation (LSC) to grid the gradients of different azimuths into the two components. Using data within a cell, the gridding formula is (Moritz 1980)

$$\mathbf{s} = \mathbf{C}_{\mathbf{sl}} \bar{\mathbf{C}}^{-1} \mathbf{l}, \quad (21)$$

where the vector $\mathbf{l}$ holds all the observed gradients within the cell, and the vector $\mathbf{s}$ holds the north and east gradient components. The matrix $\mathbf{C}_{\mathbf{sl}}$ holds the covariances between the north and east components and the observed gradients, and $\bar{\mathbf{C}}$ holds the covariances between the observed gradients, including the signal and the noise parts. The covariance function between the gradient ε_p at point p with azimuth α_p and the gradient ε_q at point q with azimuth α_q can be computed from (Hwang & Parsons 1995)

$$C_{\varepsilon\varepsilon} = C_{ll} \cos(\alpha_p - \alpha_{pq}) \cos(\alpha_q - \alpha_{pq}) + C_{mm} \sin(\alpha_p - \alpha_{pq}) \sin(\alpha_q - \alpha_{pq}), \quad (22)$$

where α_{pq} is defined by eq. (15), and C_{ll} and C_{mm} are the covariance functions for the longitudinal and transverse gradients, which are isotropic and can be modelled by using a proper model of anomaly degree variance. In this work we used the Model 4 anomaly degree variance of Tscherning & Rapp (1974) with $A = 425.28$ mgal^2, $B = 24$ and $s = 0.999617$. When gridding, the residual gradients within a $12' \times 12'$ cell around a grid point are used to compute the north and east geoid gradients. The actual covariance function used in a $12' \times 12'$ cell was obtained by applying a factor to the global covariance function of Tscherning & Rapp (1974). The factor is the ratio between the variance of the residual gradients and the variance of the global covariance function (Hwang & Parsons 1995). The use of a $12' \times 12'$ cell size was based on the comparisons between the derived and the shipborne gravity anomalies (see below). The residual gradients were weighted in inverse proportion to their squared errors in the LSC calculation. Thus it was important to estimate carefully the errors for the different altimeter missions. Table 4 shows the average errors in the geoid gradients for the altimeter missions used in this study. For the repeat missions, the errors used are the estimated standard deviations in averaging the gradients over the number of passes available. For the non-repeat data, we estimated errors using the formula

$$\sigma_g = \frac{\sqrt{2}\sigma_h}{d}, \quad (23)$$

where σ_g and σ_h are the standard deviations in the gradients and sea surface heights, respectively, and d is the distance between two successive points used for computing the gradient. Using the numbers of repeat cycles in Table 1 and the errors of the averaged gradients in Table 4, we find that the noise levels of the Geosat and ERS-1 altimeters are both 3.6 cm. Furthermore, using 111 as the number of cycles and an averaged error of 0.56 μrad, we estimate that a single T/P altimeter measurement has an accuracy of 2.4 cm.

8 THE PRODUCTION OF GLOBAL MARINE GRAVITY ANOMALIES

Fig. 5 shows a flow chart of the procedure used to determine global marine gravity anomalies. We used a $2' \times 2'$ grid size, which was primarily governed by the cross-track spacing of Geosat/GM. A $2' \times 2'$ grid size corresponds to a 3.7 km × 3.7 km spatial resolution near the equator. The cross-track spacing of ground tracks decreases when going south or north of the equator. We have done computations in areas 4 and 8 (see Fig. 4) using a $2' \times 1'$ grid size, but found no improvements in the computed gravity anomalies when

Table 4. Average errors of geoid gradients (in μrad).

Mission	Seasat	Geosat/ERM	Geosat/GM	ERS-1/35-day	ERS-1/GM	T/P
Error	10.55	0.96	7.39	1.80	7.39	0.56

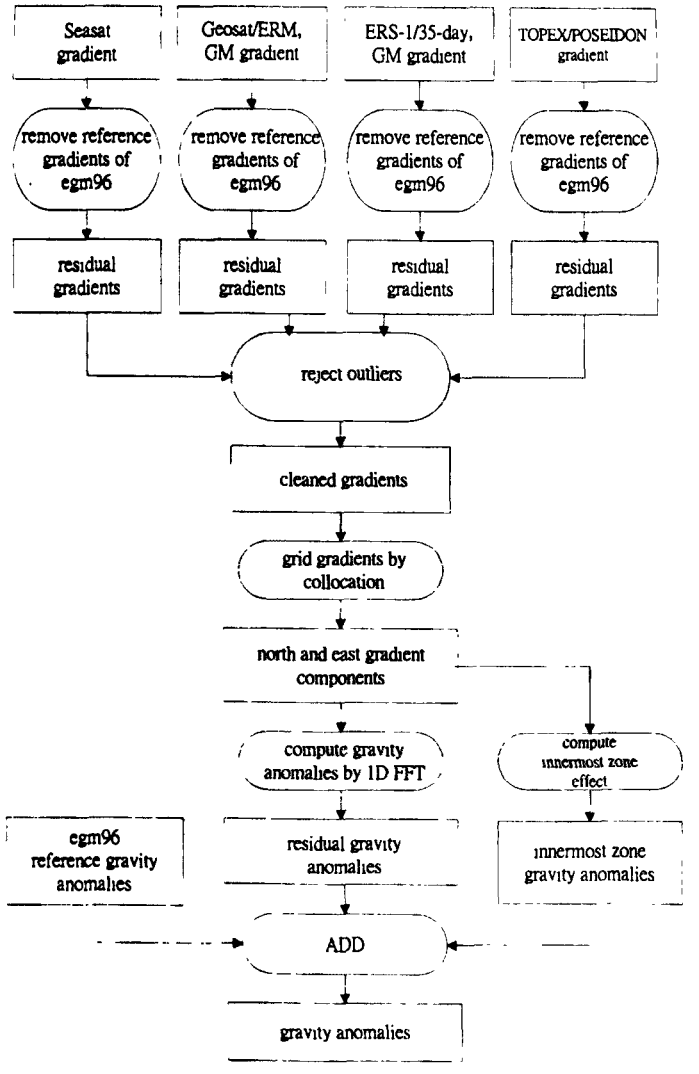

Figure 5. Flow chart for computing the global marine gravity anomalies. The rectangular boxes indicate computations and the rounded boxes indicate data sets.

comparing them with the shipborne measurements of gravity anomalies.

To produce the global 2′ × 2′ gridded gravity anomalies, we first generated global 2′ × 2′ gridded north and east components of the geoid gradient, which were then used to compute the global gravity anomalies by the 1-D FFT method. Table 5 shows typical CPU times on a Sparc20 machine for different steps of the computation in an open ocean area of size 20° × 20°. The most time-consuming parts are outlier rejection and gridding by LSC. In theory, we can compute gravity anomalies from geoid gradients by LSC (Hwang & Parsons 1995), but in this case each LSC computation would need gradients within a cell of size at least 1°, which contains about 2000 data points. This large amount of data in LSC would create difficulty in a global computation on a workstation. On the other hand, since gridding the two gradient components from the gradients of different azimuths by LSC is an interpolation process, the cell size can be relatively small. As mentioned before, in gridding the gradients we used a 12′ × 12′ cell, which typically contains about 90 points. Furthermore, since the gridded gradients were expensive to compute, they were saved for future use in an updated method for converting geoid gradients to gravity anomalies. The computations were carried out simultaneously on a cluster of workstations consisting of Sparc5, Sparc10 and Sparc20 machines and took about two weeks of CPU time in total. The final file of gravity anomaly was the result of a merger of 144 files, each covering a 20° × 20° area (the original size was 21° × 21°, which yields a 1° border to avoid bad results at the edges). The merged file covers the area from 0°E to 360°E and from 82°N to 82°S.

Table 5. Typical CPU times (in seconds) on a Sparc20 machine for different steps of the computation for an area of size 20° × 20°.

Step	Reject outliers	Grid by LSC	1D FFT
CPU time	4627	18174	459

9 COMPARISON WITH SHIPBORNE MEASUREMENTS OF GRAVITY ANOMALIES

The satellite-derived gravity anomalies were compared with the shipborne measurements of gravity anomalies from the National Geophysical Data Center (NGDC) in the 12 areas

shown in Fig. 4. Only ship data after 1980 were selected for the comparison. Before comparison, the ship gravity anomalies were adjusted to the satellite-derived gravity anomalies using a quadratic polynomial (Hwang & Parsons 1995). The result of the comparison is shown in Table 6. Table 6 also lists the result of comparing Sandwell & Smith's (1997) satellite gravity measurements with the NGDC ship gravity measurements. Except in areas 5 and 7, the rms differences from our result are smaller than those from Sandwell & Smith (1997). In general, over semi-closed seas such as the South China Sea and the Mediterranean (areas 6 and 9), the differences are larger than those in the deep oceans. Area 11 contains the Fiji Plateau and has the largest difference. These large differences suggest that more work should be done with altimeter data over shallow waters if we wish to obtain results over shallow water comparable in quality with those over the open ocean.

Table 6. Root-mean-square differences (in mgal) between the satellite-derived and the ship-measured gravity anomalies over the 12 areas.

Area	No. ship data	This work - ship	Sandwell and Smith - ship
1	16508	5.13	5.91
2	15608	6.79	7.05
3	54812	7.27	8.83
4	14885	7.04	7.39
5	68492	7.88	7.61
6	50025	10.42	10.69
7	25811	8.31	8.06
8	20736	6.93	7.36
9	118499	8.13	9.18
10	27993	7.65	7.82
11	190858	14.26	15.11
12	5270	7.47	7.77

Gravity anomalies derived for inland seas and lakes were considered separately. The Great Lakes of North America contain very few data points, so gravity computation was impossible there. Other smaller lakes in the former USSR and China have the same problem. The Black Sea and the Caspian Sea contain 36 874 and 19 700 data points, respectively, which are marginally sufficient for gravity computation. However, the data in these two areas are probably affected by serious errors in geophysical corrections, such as errors in ocean tide models. The Caspian Sea lies about 30 m below sea level and there the inverse Vening Meinesz formula may not hold. We could only acquire shipborne gravity data in the Black Sea for comparison. Fig. 6 shows the distributions of altimeter and ship data in the Black Sea. The ship-measured gravity anomalies were collected from 1967 and 1972. Because of the relatively short tracks, we did not adjust the ship data. Table 7 shows the result of the comparison for the Black Sea. If all the ship data are used for comparison, some of the points lie in shallow water, where the differences can be very large. If attention is restricted to deeper water, the differences are much smaller. In comparison with the peak-to-trough variation of 176 mgal in the gravity field for the Black Sea, the 6.77 mgal standard

Table 7. Statistics of the differences (in mgal) between ship-measured and satellite-derived gravity anomalies over the Black Sea.

	All data	Depth > 2000 m
No. ship data	3246	1199
Max	47.20	35.11
Min	-104.05	-29.75
Mean	5.53	9.57
Std. dev.	14.01	6.77

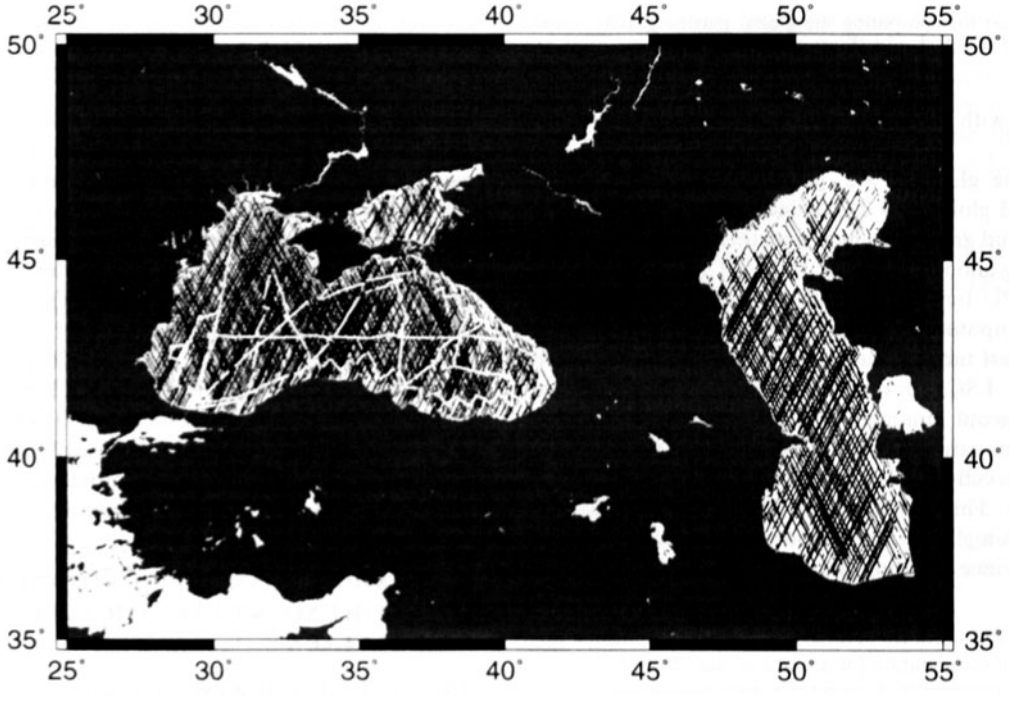

Figure 6. Distributions of altimeter data (dots, merging into dark lines) and shipborne gravity data (white lines) over the Black Sea and the Caspian Sea.

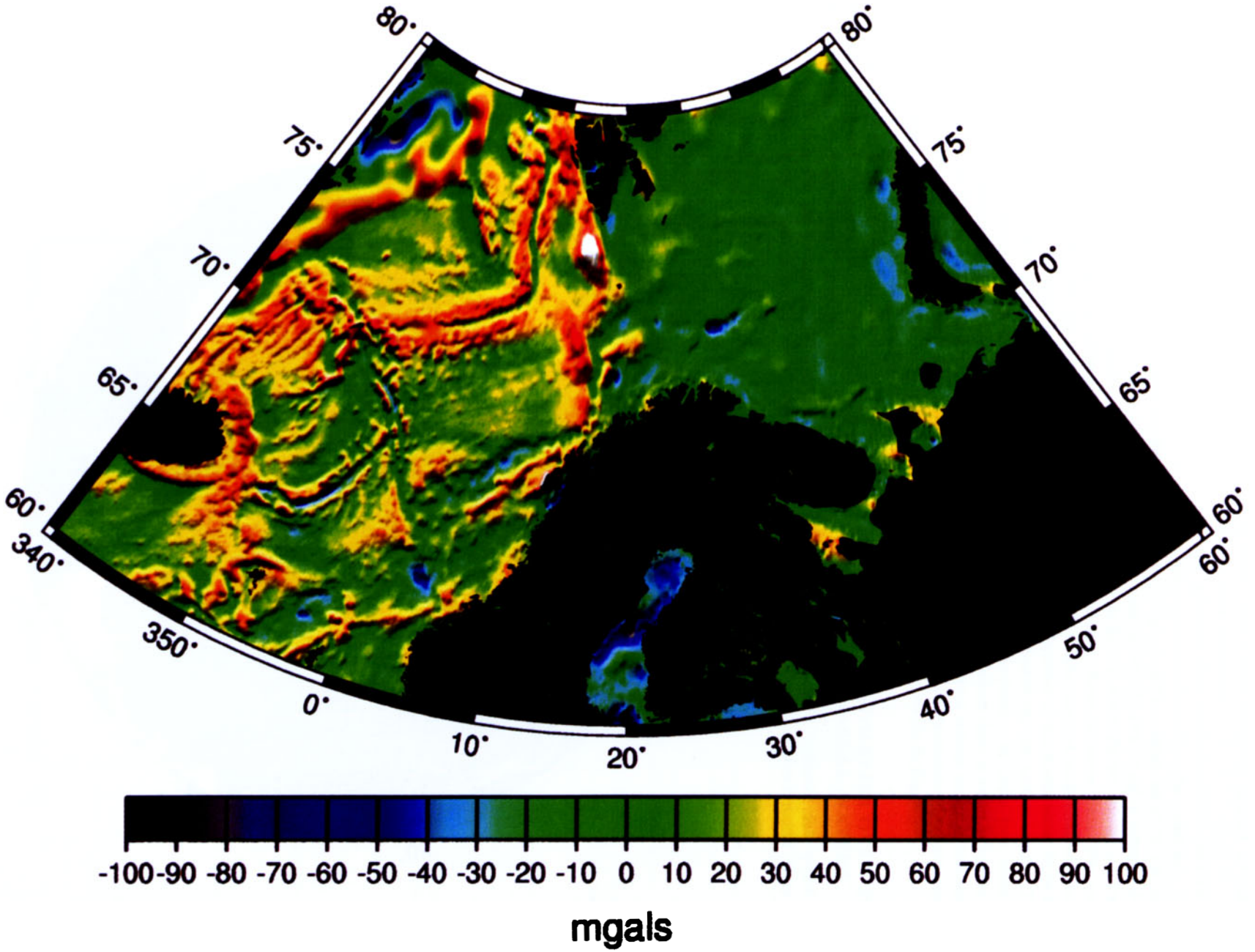

Figure 8. Colour-shaded relief map of the gravity anomalies north of the Atlantic Ocean, where many tectonic features are visible. This area is covered with relatively dense altimeter data compared to other subarctic areas.

deviation suggests that satellite altimetry is a good tool for mapping the gravity of the Black Sea.

10 GRAVITY ANOMALIES OVER ANTARCTICA AND THE ARCTIC

In the works of e.g. McAdoo & Marks (1992) and Sandwell (1992), the Antarctic gravity up to 72°S was derived from Geosat and was used for preliminary interpretations of Antarctic tectonics. The Geosat data cover most of the oceans around Antarctica, except the Weddell Sea and the area from about 170°E to 260°E [see e.g. the maps in Sandwell (1992)]. With an inclination angle of 98.5°, ERS-1 should, in addition to enhancing the spatial resolution in areas already covered by Geosat, extend the coverage to higher latitudes. However, as shown in Fig. 7, the ERS-1 data south of 72°S, except in the Ross Sea, are rather sparse and unevenly distributed. The sparsity was largely due to the elimination of altimeter data over ice-covered areas, which is one of our data-editing criteria. Note that McAdoo & Marks (1992), Sandwell (1992), Sandwell & Smith (1997) and Knudsen & Andersen (1997) did not use altimeter data over ice-covered areas for gravity anomaly derivations. In fact, the ice contamination problem can be overcome by retracking the waveforms of the altimeter; such a technique is described in e.g. Laxon (1994). Using retracked waveform data, McAdoo & Laxon (1997) and Studinger & Schoene (1997) have computed gravity anomalies of high quality over Antarctica.

The altimeter data over the Arctic also suffer ice contamination problems but with some exceptions. First, the Gulf Stream brings temperate ocean water to the subarctic area north of the Atlantic Ocean (roughly between 30°W to 80°E and 60°N to 82°N), where the sea surface is mostly free from ice and contains dense altimeter data. The vicinity of the Bering Strait is also covered with relatively dense altimeter data, perhaps because of the warm water from the Kuroshio Extension that makes the sea surface ice-free. Therefore, the derived gravity anomalies in these two areas have better accuracy and resolution than in other subarctic areas. As an example, Fig. 8 shows a colour image of the satellite-derived gravity north of the Atlantic Ocean. Many pronounced tectonic signatures are clearly visible in Fig. 8.

11 GRAVITY ANOMALIES OVER SHALLOW WATERS AND COASTAL WATERS

Over shallow waters, the altimeter data could be seriously affected by a bad wet tropospheric model, large ocean waves

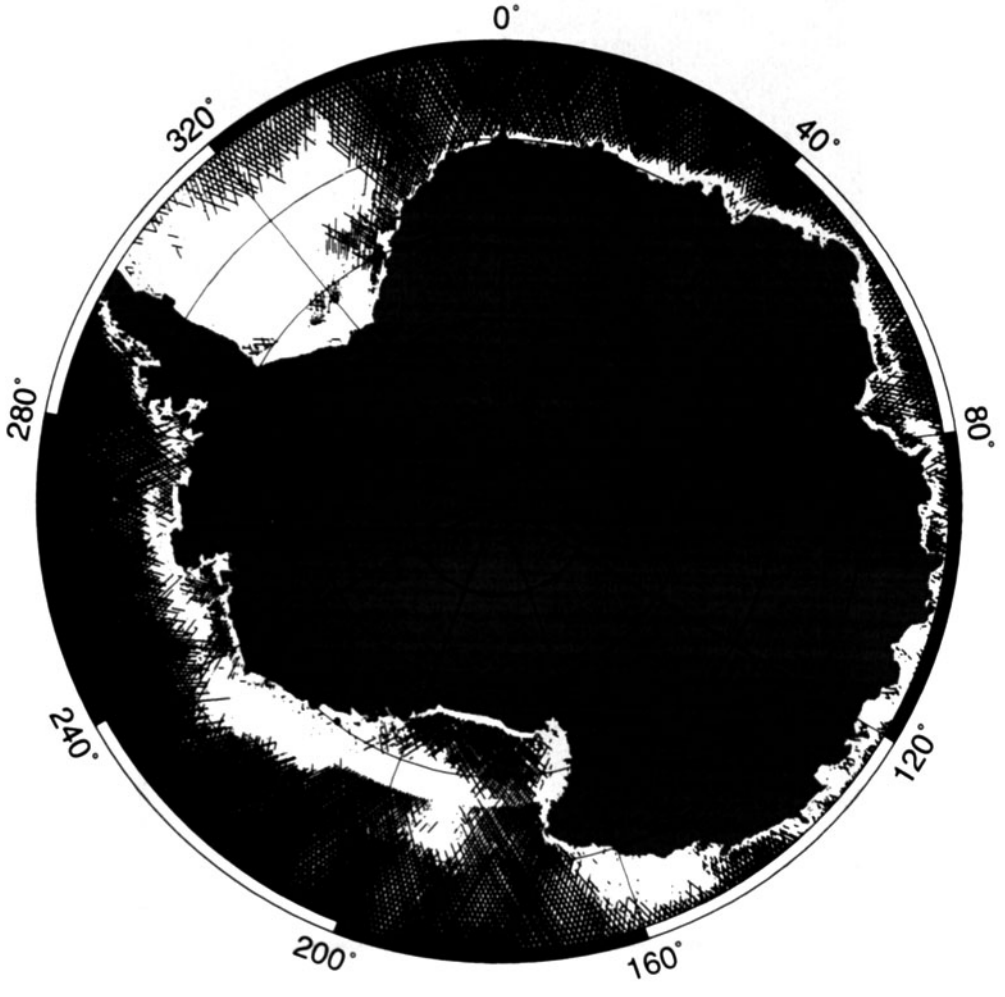

Figure 7. Distribution of ERS-1/35-day and ERS-1/GM altimeter data over Antarctica. The location of the Ross Sea is shown in Fig. 4 (area 12). The latitudes start from −65° and are annotated at a 5° tick interval.

and unmodelled tidal constituents; going further to coastal waters, additional damage could come from distorted altimeter waveforms due to returns from the ground. The radii of the altimeter footprints of Seasat, Geosat, ERS-1 and T/P are 1.6–12 km, 9.6 km, 1–2 km and 10 km, respectively (Seeber 1993). [Note that the radii increase over rough sea, see Rummel (1993), p. 195]. These radii are the minimum distances to land that are required for undistorted waveforms. In fact, for good altimeter data, the minimum 'safe' distance to land should be much larger than the radius of the footprint. For example, the radiometer footprint of T/P is around 30 km, so the T/P observed sea surface heights with distances to land less than 30 km will have bad tropospheric corrections and will be very inaccurate (C. K. Shum, personal communication, 1998). In addition, gravity computation near coastal waters near a continent will be theoretically inaccurate because there are no altimeter data on the continent (eq. 15 requires evenly distributed data around a computational point). Thus, in order to get good gravity anomalies from altimetry over coastal waters, we should (1) improve the quality of coastal altimeter data, and (2) obtain data such as land gravity anomalies and geoidal heights from GPS and levelling in the immediate vicinity of the coastal waters. In the latter case, since the data used are heterogeneous, one would have to use LSC to compute gravity anomalies. Therefore, one would expect that the derived gravity anomalies over shallow waters and coastal waters would not have the same accuracy and resolution as in the open ocean. In fact, we suggest applying a filter or data-editing to gravity anomalies before use in these two cases. As an example, we applied a median filter with a wavelength of 7.4 km to the gravity anomalies over the continental shelf (defined as the area with depth less than 300 m) of East Asia. Fig. 9 shows the distribution of those differences between the raw and the filtered gravity anomalies that are larger than 5 mgal. Most of the large differences occur along the coastal waters, and some even reach 100 mgal.

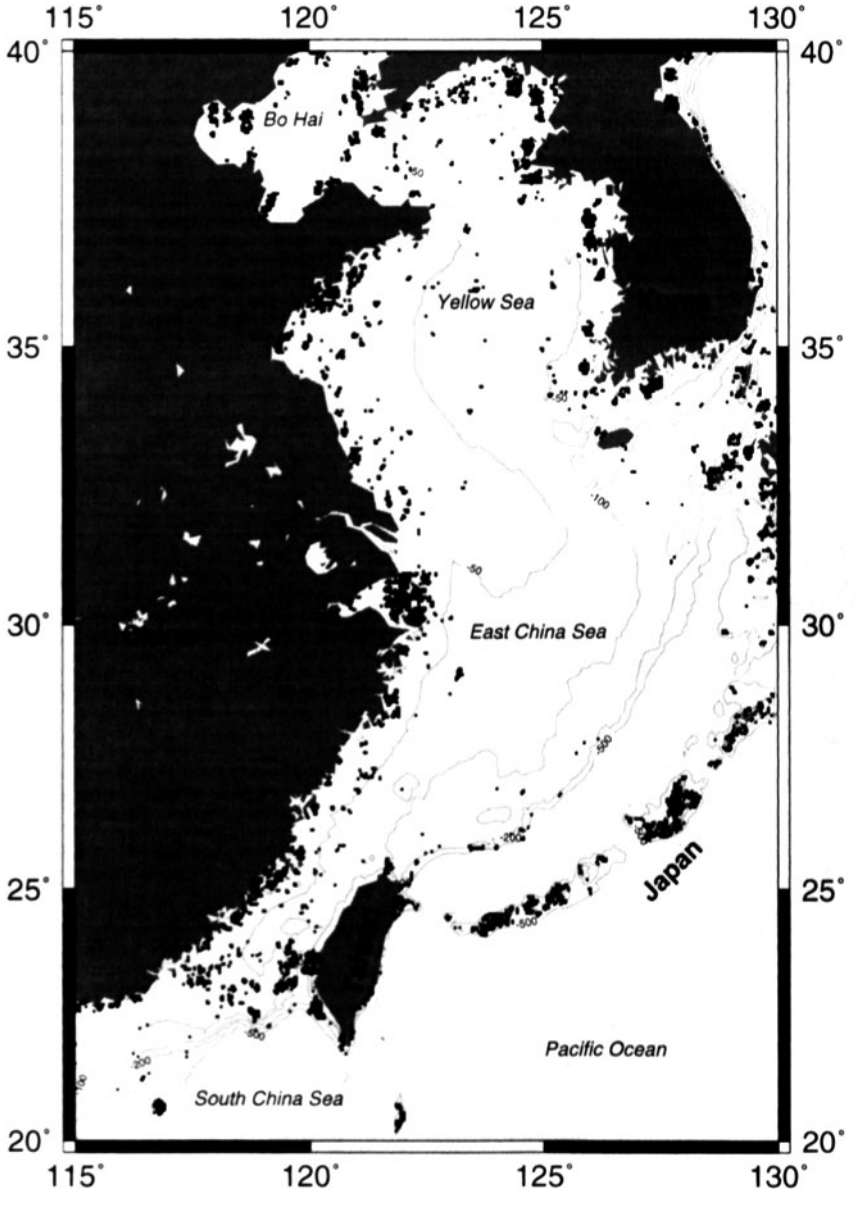

Figure 9. Distribution (black dots) of those differences between the raw and filtered gravity anomalies that are larger than 5 mgal over the continental shelf of East Asia; dotted contours indicate depths.

12 CONCLUSIONS

This paper shows the data, procedure and quality evaluation in our global computation of marine gravity anomalies from multisatellite altimetry. Such a computation will be repeated in the future and we will include additional data from new missions such as ERS-2, Geosat-Follow-On and JASON-1, and use updated existing data. Indeed, for the existing data, there are many areas that could be improved substantially. For example, a model to remove the time-varying sea surface topography is needed for the non-repeat missions. Over coastal waters, techniques must be developed to retrack the returned waveforms of the altimeter so that here the data can be useful for gravity derivation; one such technique is reported by Nuth *et al.* (1997). An improved tide model not solely derived from altimetry is also required, especially for shallow waters. In addition to the applications illustrated in Sandwell & Smith (1997), the gravity anomalies described in this study can also be used to derive mean gravity anomalies for modelling high-degree geopotential coefficients, and to study the spectral properties of the Earth's gravity field.

ACKNOWLEDGMENTS

This research was supported by the National Science Council of the Republic of China, under contract NSC86-2611-M-009-001-OS. The free software GMT (Wessel & Smith 1995) was used to display most of the data.

REFERENCES

Cheney, R.E., Doyle, N.S., Bruce, B.C., Agreen, R.W., Miller, L., Timmerman, E.L. & MacAdoo, D., 1991. *The Complete Geosat Altimeter GDR Handbook,* Office of Ocean and Earth Sciences, NOAA National Ocean Service, Rockville, Maryland.

Eanes, R. & Bettadpur, S., 1995. *The CSR 3.0 Global Ocean Tide Model,* CSR-TM-95-06, Center for Space Research, University of Texas, Austin.

Haagmans, R., de Min, E. & von Gelderen, M., 1993. Fast evaluation on convolution integrals on the sphere using 1D FFT, and a comparison with existing methods for Stokes' integral, *Manuscripta Geodaetica,* **18,** 227–241.

Haxby, W.F., Karner, G.D., LaBrecque, J.L. & Weissel, J.K., 1983. Digital images of combined oceanic and continental data sets and their use in tectonic studies, *EOS, Trans. Am. geophys. Un.,* **64,** 995–1004.

Hwang, C., 1989. *High precision gravity anomaly and sea surface height estimation from Geos-3/Seasat altimeter data,* Report 399, Dept of Geodetic Science and Surveying, Ohio State University, Columbus, Ohio.

Hwang, C., 1997. Analysis of some systematic errors affecting altimeter-derived sea surface gradient with application to geoid determination over Taiwan, *J. Geodyn.,* **71,** 113–130.

Hwang, C., 1998. Inverse Vening Meinesz formula and deflection-geoid formula: applications to the predictions of gravity and geoid over the South China Sea, *J. Geodyn.,* in press.

Hwang, C. & Parsons, B., 1995. Gravity anomalies derived from Seasat, Geosat, ERS-1 and TOPEX/POSEIDON altimetry and ship gravity: a case study over the Reykjanes Ridge, *Geophys. J. Int.,* **122,** 551–568.

Hwang, C. & Parsons, B., 1996. An optimal procedure for deriving marine gravity from multi-satellite altimetry, *Geophys. J. Int.,* **125,** 705–719.

Kaula, W.M., 1966. *Theory of Satellite Geodesy,* Blaisdell, London.

Knudsen, P. & Andersen, O.B., 1997. Global marine gravity field from geodetic mission altimetry, *J. geophys. Res.,* in press.

Laxon, S., 1994. Sea ice altimeter processing scheme at the EODC, *Int. J. remote Sensing,* **15,** 915–924.

Le Traon, P.Y., Caspar, P., Bouyssel, F. & Makhmara, H., 1995. Using TOPEX/POSEIDON data to enhance ERS-1 orbit, *J. atmos. oceanic Technol.,* **12,** 161–170.

Lemoine, F.G. *et al.,* 1997. The development of the NASA/GSFC and NIMA Joint Geopotential Model, *Proc. Int. Symp. on Gravity, Geoid and Marine Geodesy, Tokyo,* eds Segawa, J., Fujimoto, H. & Okubo, S.

Levitus, S., 1982. *Climatological Atlas of the World Ocean,* NOAA Professional Paper 13, US Dept of Commerce, Rockville, Maryland.

McAdoo, D.C. & Laxon, S., 1997. Antarctic tectonics: constraints from an ERS-1 satellite marine gravity field, *Science,* **276,** 556–560.

McAdoo, D.C. & Marks, K., 1992. Gravity over the southern ocean from Geosat data, *J. geophys. Res.,* **97,** 3247–3260.

Moritz, H., 1980. *Advanced Physical Geodesy,* Abacus Press, Karlsruhe.

Nuth, V., Wilson, C.R., Kruzinga, G. & Shum, C.K., 1997. The use of altimeter data in the coastal waters, *EOS, Trans. Am. geophys. Un.,* **78,** 104.

Pope, A.J., 1976. *The Statistics of Residuals and Detection of Outliers,* TR. NOS. 65 NGS. 1, NOAA, National Ocean Service, Rockville, Maryland.

Rapp, R.H. & Basic, T., 1992. Oceanwide gravity anomalies from Geos-3, Seasat and Geosat altimeter data, *Geophys. Res. Lett.,* **19,** 1979–1982.

Rapp, R.H., Wang, Y.M. & Pavlis, N., 1991. *The Ohio State 1991 geopotential and sea surface topography harmonic coefficient models,* Report 410, Dept of Geodetic Science and Surveying, Ohio State University, Columbus, Ohio.

Rummel, R., 1993. Principle of satellite altimetry and elimination of radial orbit errors, in *Lecture Notes in Earth Sciences,* Vol. 50, pp. 190–241, eds Rummel, R. & Sansò, F., Springer, Berlin.

Sandwell, D.T., 1992. Antarctic marine gravity field from high density satellite altimetry, *Geophys. J. Int.,* **109,** 437–448.

Sandwell, D.T. & Smith, W.H.F., 1997. Marine gravity anomaly from Geosat and ERS 1 satellite altimetry, *J. geophys. Res.,* **102,** 10 039–10 054.

Seeber, G., 1993. *Satellite Geodesy: Foundations, Methods, and Applications,* Walter de Gruyter, New York.

Studinger, M. & Schoene, T., 1997. Geotectonics of the Weddell Sea, Antarctica: results and interpretations from ERS-1 and Geosat derived gravity maps, *EOS, Trans. Am. geophys. Un.,* **78,** 103.

Tscherning, C.C. & Rapp, R.H., 1974. *Closed covariance expressions for gravity anomalies, geoid undulations and deflections of the vertical implied by anomaly degree variance models,* Report 208, Dept of Geodetic Science and Surveying, Ohio State University, Columbus, Ohio.

Wang, Y.M., 1993. On the optimal combination of potential coefficient model with terrestrial gravity for FFT geoid computation, *Manuscripta Geodaetica,* **18,** 406–416.

Wessel, P. & Smith, W.H., 1995. New version of the generic mapping tools released, *EOS, Trans. Am. geophys. Un.,* **76,** 329.